A Modular Layer-by-Layer Nanoparticle Platform for Hematopoietic Progenitor and Stem Cell Targeting

Authors: Tamara G. Dacoba[1], Namita Nabar[1,2], Paula T. Hammond[1,2,3,4,*]

Affiliations:

[1]Koch Institute for Integrative Cancer Research, Massachusetts Institute of Technology; Cambridge, MA 02142, USA.

[2]Department of Chemical Engineering, Massachusetts Institute of Technology; Cambridge, MA, 02142, USA

[3]Broad Institute of MIT and Harvard; Cambridge, MA 02142, USA.

[4]Institute for Soldier Nanotechnologies, Massachusetts Institute of Technology; Cambridge, MA 02139, USA.

*Corresponding author: hammond@mit.edu

Keywords: hematopoietic stem cells, targeting, stealth nanoparticles, hematological malignancies, in vivo targeting

Abstract:

Effective delivery of drugs and gene editing cargos to hematopoietic stem and progenitor cells (HSPCs) is a major challenge. Current therapeutic strategies in genetic disorders or hematological malignancies are hindered by high costs, low accessibility, and high off-target toxicities. Layer-by-Layer nanoparticles (LbL NPs) are modular systems with tunable surface properties to enable highly specific targeting. In this work, we developed LbL NPs that target HSPCs via antibody functionalization with reduced off-target uptake by circulating myeloid cells. NPs layered with poly(acrylic acid), a bioinert polymer, provided more stealth properties in vivo than other tested bioactive polyanions. The additional conjugation of anti-cKit and anti-CD90 antibodies improved NP uptake by 2- to 3-fold in non-differentiated bone marrow cells in vitro. By contrast, anti-CD105 functionalized NPs showed the highest association to HSPCs in vivo, ranging from 3.0–8.5% in progenitor subpopulations. This LbL NP platform was then adapted to target human HSPC receptors, with similar targeting trends in healthy CD34+ human cells. In blood disorders, anti-CXCR4 functionalization demonstrated the greatest targeting to B-cell lymphoblasts. Taken together, these results underscore the therapeutic potential of this modular LbL NP platform with the capacity to target HSPCs in a disease-dependent context.

INTRODUCTION

Hematopoietic stem and progenitor cells (HSPCs) are the precursors of all blood cell lineages.[1] Any mutations or defects affecting these cells results in numerous blood diseases, such as hemoglobinopathies (e.g., beta-thalassemia, sickle cell disease), immune diseases, storage and metabolic disorders, or blood malignancies (e.g., acute myeloid leukemia, multiple myeloma).[2,3] HSPCs possess self-renewal and multipotency, making them invaluable therapeutic targets to treat any of these disorders at the source. However, manipulating HSPCs is challenging sue to their limited numbers and confinement within the bone marrow niche.[4]

Current clinical interventions for these disorders involve hematopoietic stem cell transplantation, with important limitations.[5] In particular, ex vivo gene editing and re-infusion of HSPCs is a very technical and costly process –of over $2M per patient–, which hinders the accessibility to the general population.[6] Besides, these and other therapies in clinical evaluation employ viral vectors or electroporation, with known limitations.[2,7,8] In the case of hematological malignancies, chemotherapeutics or small molecule inhibitors present broad organ biodistribution and poor specificity, causing serious side effects in healthy tissues.[9,10] Thus, to avoid costly and complex ex vivo cell processing, while decreasing in vivo toxicities and enabling broader therapeutic applications in HSPC engineering, the development of a targeted nanomedicine delivery system to manipulate HSPCs is needed.[11,12]

In this regard, nanoparticles (NPs) have the capacity to deliver a great variety of drug cargos, while reducing off-target toxicity and improving drug biodistribution.[13,14] Our lab has leveraged the layer-by-layer (LbL) assembly method to enable tunable surface properties of NPs by electrostatic deposition of alternating polyelectrolytes, driving improvements in targeting specificity and biodistribution.[15,16] The LbL NP construct's modularity allows the NP core to be switched based on the cargo of interest, with liposomes,[17–19] polymeric NPs,[20] and lipid nanoparticles (LNPs),[21] amenable to this surface modification. These LbL NPs can be further directed to cells and tissues of interest by adsorbing targeting moieties,[22] conjugating peptides[23,24] or antibodies to their surface.[25]

HSPC-targeting strategies have so far leveraged many different antibodies (Abs) to deliver therapies to these cells. For instance, CD45, a universal hematopoietic marker expressed in HSPCs and differentiated immune cells, has been targeted both by antibody-drug conjugates or Ab–LNPs for gene delivery applications.[26–28] The cKit (CD117) receptor, expressed on hematopoietic progenitors, has prompted the use of anti-cKit Abs conjugated to LNPs to enhance targeting and gene editing in mouse and human HSPCs.[29–31] This tyrosine kinase receptor is known for its role in HSPC proliferation, survival, and differentiation.[32] However, recently reported adverse effects—including the death of a patient—have raised safety concerns around using anti-cKit systems, highlighting the need for alternative targets.[33] Another candidate, CXCR4 (CD184), is involved in HSPC homing in the bone marrow niche, which has led to the clinical use of its antagonists as HSPC-mobilization agents. [34–36] Additional HSPC-targeting Abs include CD90 (Thy1) and CD105 (endoglin), which have shown success with both targeted lentiviral vectors and NPs.[37–40] CD90, a cell surface protein, is expressed by various cell types, including primitive HSPCs.[41] CD105, part of the TGF-β receptor complex, is primarily expressed by endothelial cells but also by subsets of HSPCs, where it promotes stemness.[39,42] Despite these advancements,

no studies have systematically compared the benefits and limitations of targeting these hematopoietic receptors across both healthy and diseased conditions.

In this work, we evaluate the potential of the LbL NP platform to develop a targeted system for drug delivery to HSPCs. We hypothesize that we can leverage the modularity of LbL NPs to compare and assess different surface properties for HSPC targeting. We first explore different surface polymers for their ability to decrease unwanted LbL NP interactions with circulating myeloid cells.[6] Upon selection of poly(acrylic acid) (PAA) as the stealth layer, we further modify the surface of PAA NPs with HSPC-targeting Abs, systematically comparing several promising candidates: anti-cKit, anti-CD45, anti-CXCR4, anti-CD90, and anti-CD105. In vitro studies in mouse bone marrow cells demonstrate the impact of Ab on LbL NP uptake and trafficking patterns across Ab targets, with anti-cKit and anti-CD90 improving NP uptake the most. In vivo, anti-CD105 functionalization causes the greatest association to murine HSPCs. To assess the potential translation of these targets, we utilize human CD34+ cells to confirm that anti-human CD105 also increases LbL NP association in vitro. Anti-CXCR4 functionalization confers advantages in disease settings, as it improves LbL NP association in CXCR4-overexpressing human leukemia lines. Overall, we have harnessed the modularity of LbL NPs to develop a platform with stealth properties that, upon the conjugation of a targeting moiety, can efficiently reach different hematopoietic targets in vitro and in vivo.

RESULTS

Outer layer selection impacts uptake by circulating myeloid cells in vivo

Myeloid cells such as granulocytes and monocytes exert a critical function in immune surveillance by clearing any foreign body –as NPs– from systemic circulation. To prevent this rapid clearance, we first aimed to identify an LbL NP outer layer that would limit the interactions with these cells. For this, we layered negatively charged fluorescently-labeled liposomes sequentially with the polycation poly-L-arginine (PLR), and a polyanion: hyaluronic acid (HA), poly-L-glutamic acid (PLE), or poly(acrylic acid) (PAA) (Fig. 1A). After each layer deposition, nanoparticle size increased by 5–30 nm and LbL NP charge converted, yielding final LbL NPs of less than 150 nm, low PDIs, and negative surface charge (Fig. 1B, C). We evaluated LbL NP interactions with circulating immune cells and organ biodistribution 1.5 h after intravenous administration in healthy Black-6 mice (Fig. 1D and Suppl. Fig. 1). Among LbL chemistries, no significant differences were observed in the relative abundances of each cell subpopulation (Fig. 1E). Similarly, the LbL NP association to circulating CD45+ cells was comparable among groups (Fig. 1F). However, the distribution of cells within NP-positive populations did significantly change for the tested LbL NPs (Fig. 1G and Suppl. Fig. 2). For instance, HA NP-positive cells were enriched in granulocytes and monocytes (46.9% and 11.6%, respectively); while bare NP-positive cells were comprised of 26.5% and 2.1%, and PLE NP-positive cells of 24.6% and 8.3%. In contrast, only a 13.9% and 4.5% of PAA NP-positive cells were identified as granulocytes and monocytes. Consequently, a higher portion of PAA NP-positive cells were B cells (74.7%), which resembles their abundance in mouse blood (63.5% in control mice) (Fig. 1E, G). Interestingly, 4.3% of HA NP-positive cells were T cells, higher than within PLE-, PAA-, and bare NP-positive cells (2.0%, 1.5%, 0.9%, respectively), highlighting the specificity of HA toward T cells. On an organ level, all NPs were

present in the liver to a similar extent, and PAA NPs presented the lowest accumulation in all the other organs profiled (Fig. 1H and Suppl. Fig. 3). Collectively, the reduction in myeloid cells association and the lowered organ accumulation led to the selection of PAA as the stealth outer layer of the Ab-LbL NPs used in this work.

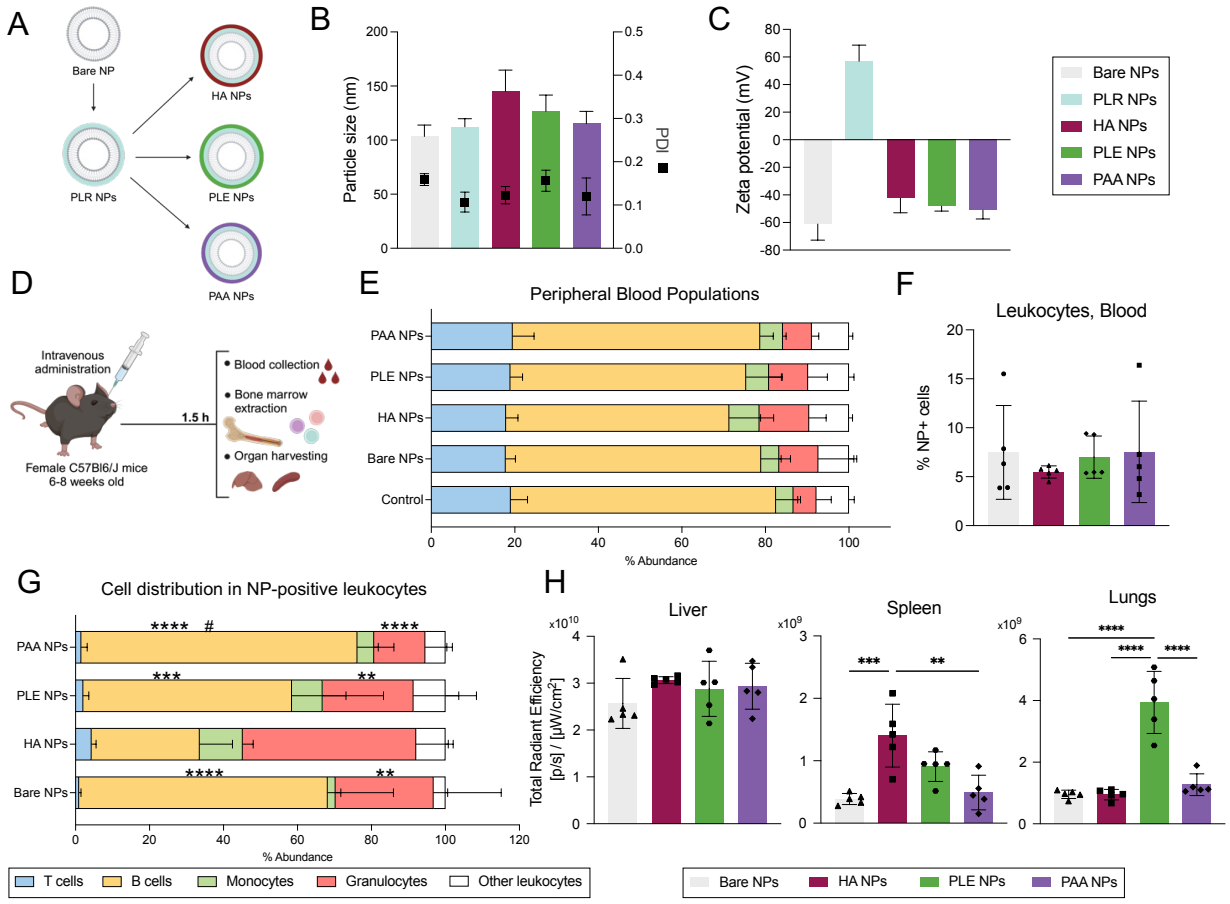

Fig. 1. Biodistribution of LbL NPs with HA, PLE, and PAA as outer layers in circulating blood cells and major organs. (**A**) Schematic of the layering construction, starting with a liposome (bare NP), then layering with the polycation PLR, and finally with three different polyanions: HA, PLE, or PAA. (**B, C**) Average particle size (Z-average), polydispersity index (PDI) and ζ-potential of the different LbL NPs. (**D**) Timeline of in vivo study, in which NPs are intravenously administered to mice, and after 1.5 h the blood and organs are analyzed. (**E**) Blood cell composition in the different treatment groups, in terms of B cells, T cells, monocytes, granulocytes, and other leukocytes. (**F**) LbL NP association with all CD45+ leukocytes for the different treatment groups; bars represent the mean, and each dot one biological replicate. (**G**) Blood cell distribution of these NP-positive cells for the different cell subtypes. Statistical analysis is a two-way ANOVA with Tukey correction (* are differences compared to HA NP group and # to PLE NP group; *p<0.05, **p<0.01, ***p<0.005, ****p<0.001); n=5 mice per group. (**H**) Radiant efficiency measurements obtained via IVIS of the fluorophore (Cy5)-tagged LbL NPs in liver, spleen, and lungs; bars represent the mean, and each dot represents one biological replicate; n=5 mice per group. Statistical analysis is a one-way ANOVA with Tukey correction (**p<0.01, ****p<0.001).

Antibody-functionalized layer-by-layer nanoparticles

To covalently attach Abs to PAA NPs, we modified around 2.5% of the carboxylic acid groups of PAA with a methyltetrazine amine (mTz) handle, to facilitate an orthogonal reaction with trans-cyclooctene (TCO)-modified Abs (Suppl. Fig. 4). We selected five different HSPC targets: cKit, CD45, CXCR4, CD90, and CD105; generating a library of anti-mouse Ab-functionalized PAA NPs (Ab–PAA NPs) with a non-targeting isotype control (ISOT–PAA NP) (Fig. 2A). In all cases, Abs were partially reduced to expose a low number of thiols, and subsequently functionalized via maleimide-thiol chemistry with a bifunctional PEG spacer (maleimide–PEG_3–TCO) (Fig. 2B). All Abs had an average of 1-2 linkers (Fig. 2C). To construct the targeted delivery system, we layered PLR NPs with a 50/50 blend of PAA and mTz-PAA, resulting in ~120 nm particle sizes, with low PDI, and negative surface charge (Fig. 2D, E). A high Ab conjugation yield (>80%) was achieved across all groups (Fig. 2F). Cryo transmission electron microscopy images of PAA NPs and cKit–PAA NPs confirm the NP structure was maintained after functionalization (Fig. 2G and Suppl. Fig 5A). The association of Abs to the surface of PAA NPs was further confirmed through staining with 6-nm gold NPs functionalized with a binding fragment.[43,44] Using polystyrene NPs as the core, gold NPs were detected on the surface of Ab–PAA NPs, in comparison to PAA NPs (Fig. 2H and Suppl. Fig 5B). By analyzing the number of gold NPs per PAA NP, we calculated that approximately 45 Abs are conjugated per NP. Overall, through optimized surface chemistry and conjugation, we have developed a highly modular Ab–LbL NP template to evaluate a broad library of HSPC-targeting Abs.

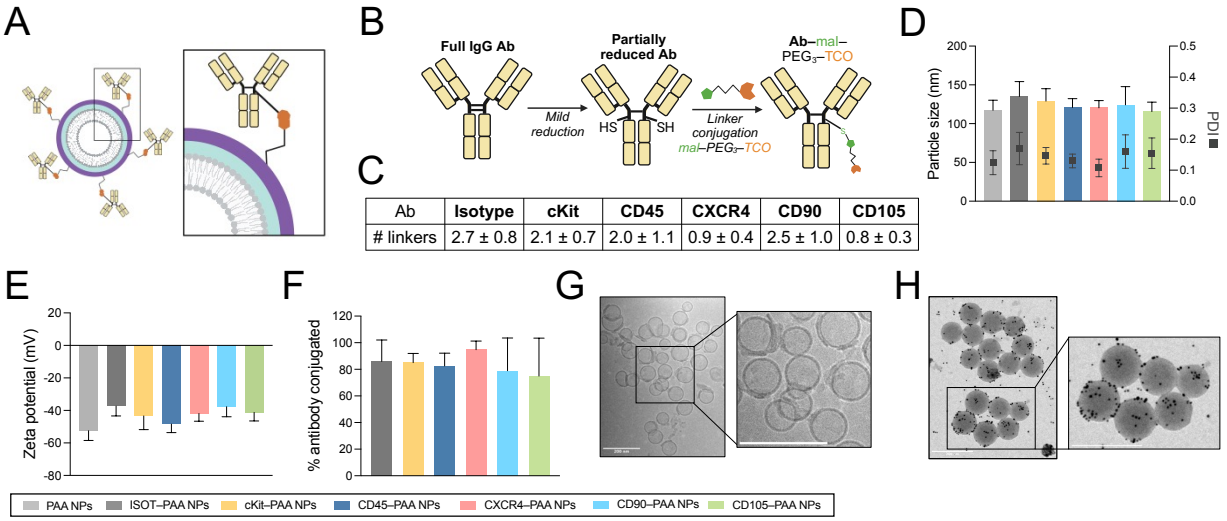

Ab	Isotype	cKit	CD45	CXCR4	CD90	CD105
# linkers	2.7 ± 0.8	2.1 ± 0.7	2.0 ± 1.1	0.9 ± 0.4	2.5 ± 1.0	0.8 ± 0.3

Fig. 2. Development of Ab–PAA NPs. (**A**) Schematic of an Ab–LbL NP, zooming into the Ab conjugated through the hinge region to the chemical handles presented on the outer layer polymer. (**B**) Ab modification reaction, where a full IgG Ab is reduced to free the thiol groups in the hinge region and then reacted to a bifunctional linker. (**C**) Table summarizing the number of linkers conjugated to each Ab (n≥3 replicates). (**D, E**) Average particle size (Z-average), polydispersity index (PDI), and ζ-potential of the library of Ab–PAA NPs. (**F**) Yield of the conjugation reaction after purification of the five Abs and control isotype. Bars represent mean ± standard deviation (n≥3 replicates). (**G**) Cryo transmission electron microscopy images of cKit–PAA NPs. (**H**) Transmission electron microscopy images of cKit–PAA NPs (with a 100-nm polystyrene core) stained with 6-nm gold NPs. Scale bars represent 200 nm.

In vitro hematopoietic progenitor cell targeting

To better understand the interactions of the selected Abs with the targeted cells, we characterized the expression of Abs' corresponding receptors on freshly harvested mouse whole bone marrow (WBM) cells and in progenitor-like lineage-depleted (Lin-) cells (Fig. 3A). In both populations, the CD45 receptor was highly expressed, as expected for this universal hematopoietic marker.[27] Receptor expression was higher for the other Abs in Lin- cells compared to WBM cells, confirming the specificity of these receptors in progenitor-like populations (Fig. 3B).

Next, we evaluated the association of PAA NPs and Ab–PAA NPs to WBM at shorter time points (0.5 and 1.5 h) to focus on specific, receptor-mediated uptake, since LbL NPs have consistently resulted in high NP uptake rates at 4 h in a variety of cells.[45] Flow cytometry showed that anti-cKit and anti-CD90 functionalization yielded the highest NP association to both WBM and Lin- cells (Fig. 3C and Suppl. Fig 6A, B). In Lin- cells, NP association at 1.5 h increased by 2.0- and 3.3-fold with cKit– and CD90–PAA NPs, in comparison to PAA NPs (Fig. 3C). We confirmed this effect was driven by the conjugation of the Abs to PAA NPs, and not by the net presence of the Abs mixed with PAA NPs (Fig. 3D and Suppl. Fig. 6C).

We then characterized the trafficking of Ab–PAA NPs in WBM cells by confocal microscopy. We tracked both the NP core (Cy5-tagged lipid) and the targeting Ab (secondary Ab staining) at 1.5 h of incubation. Low NP-cell interaction was visualized for untargeted PAA NPs and ISOT–PAA NPs (Fig. 3E). For cKit– and CD105–PAA NPs, both NPs and Abs were detected inside the cells and associated to their membrane. A strong Ab and NP signal on the surface of WBM cells was detected for CD45–PAA NPs, correlating with the high CD45 expression in cells of hematopoietic origin (Fig. 3B). Although flow cytometry indicated a more potent association for CD90–PAA NPs, both CXCR4– and CD90–PAA NPs were similarly co-localized with the cell membrane (Fig. 3E). Functionalization of PAA NPs with HSPC-targeting Abs results in important uptake and trafficking patterns in bone marrow populations, demonstrating the role of the targeting moiety on the performance of Ab–PAA NPs.

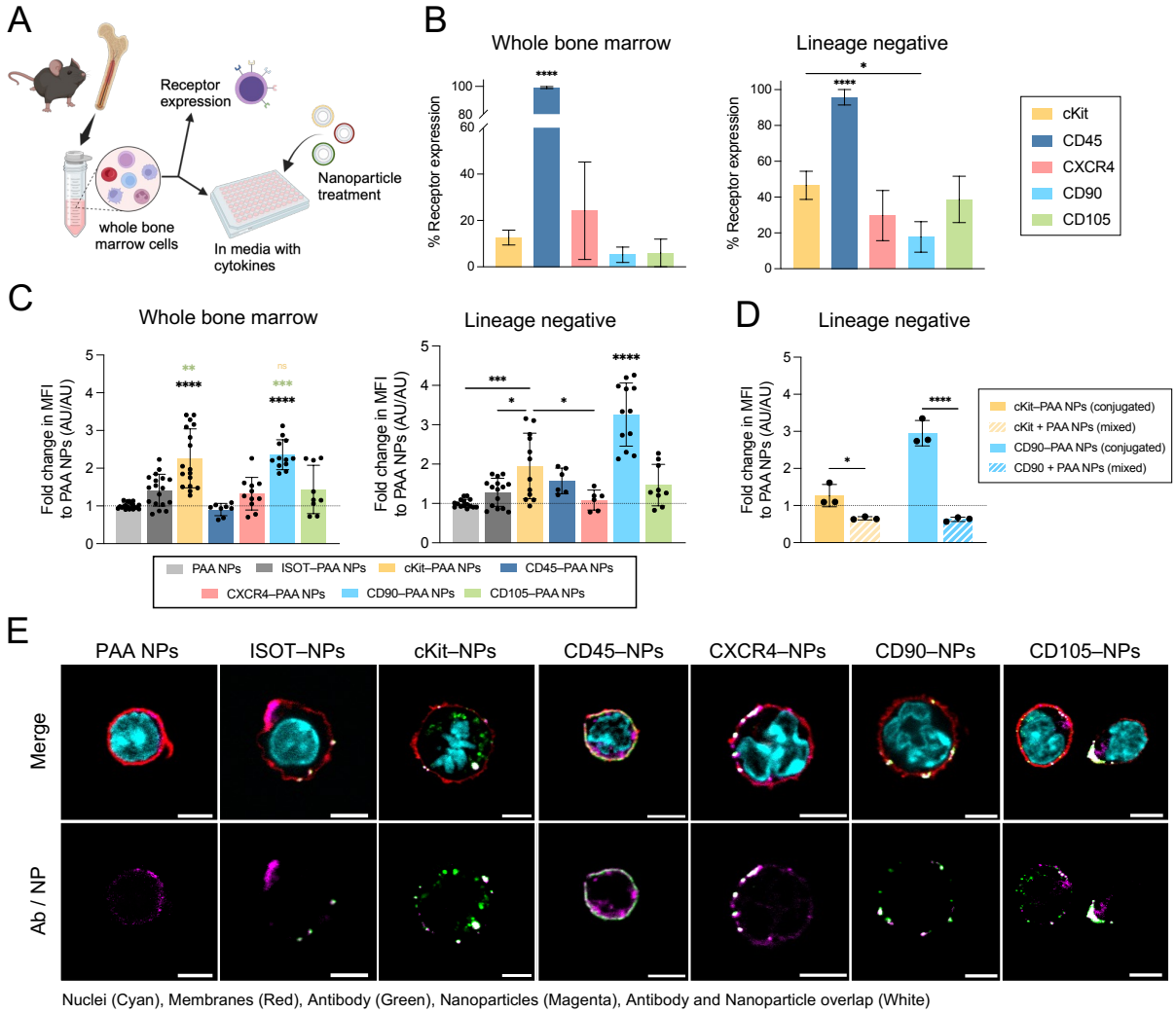

Fig. 3. Evaluation of Ab-functionalized PAA NPs in bone marrow cells. (**A**) Bone marrow cells were freshly harvested, to measure receptor expression or to be treated with Ab–LbL NPs. (**B**) Expression of receptors for each targeting Ab in WBM cells and Lin- cells. (**C**) Median fluorescence intensity (MFI) values for all groups after 1.5 h of incubation with WBM cells or Lin- cells, normalized to PAA NP. Statistical analysis is a one-way ANOVA with Tukey correction (*$p<0.05$, ***$p<0.005$, ****$p<0.001$). Each point is one technical replicate (≥3 biological replicates, each with 3 technical replicates). (**D**) Median fluorescence intensity (MFI) values after 1.5 h of incubation of Ab–PAA NPs or PAA NPs with unconjugated Ab in Lin- cells, normalized to PAA NP. (**E**) Representative confocal images of WBM cells that were treated with Ab–PAA NPs for 1.5 h. Top images represent the merge of all the color stains, and the bottom images show the NP core (Cy5-tagged lipid) and Ab (secondary antibody) stains. Scale bars represent 5 μm.

Anti-CD105 functionalization improves HSPC-targeting capacity of PAA NPs in vivo

Next, we investigated the targeting capacity of the Ab–PAA NPs in vivo. In this study, we injected the Ab–LbL NPs intravenously, then collected blood, bones, and major organs at 1.5 h for further analysis (Fig. 4A). Hematopoietic subpopulations, from Lin- to hematopoietic progenitors, were identified via flow cytometry (Fig. 4B and Suppl. Fig. 7). Aligning with previous in vitro results, both

CD45–PAA NPs and CXCR4–PAA NPs did not show any improved targeting capacity in comparison to the ISOT–PAA NP control, or untreated mice (Fig. 4C and Suppl. Fig. 8). A generally higher Ab–PAA NP uptake by all bone marrow cell populations was observed for cKit–, CD90–, and CD105–PAA NPs. Among WBM, Lin-, and Lin- Sca-1+ cKit+ (LSK) populations, both anti-CD90 and anti-CD105 had improved targeting capacities over their counterparts. For multipotent progenitors (MPPs) and hematopoietic stem cells (HSCs), CD105–PAA NPs presented a clear improvement over all the other candidates, associating with 2.7% of MPPs, 3.8% of granulocyte/monocyte MPPs, 8.5% of megakaryocyte/erythrocyte MPPs, and 3.0% of HSCs (Fig. 4C and Suppl. Fig. 8). Both CD90– and cKit–PAA NPs also showed higher association to MPPs and HSCs than did the ISOT–PAA NPs, albeit not to a statistically significant degree. To note, the low numbers of MPPs and HSCs profiled cause high variability between animals. Furthermore, the cKit receptor expression was significantly reduced in mice that received the cKit–PAA NPs, due to the quick internalization of the receptor and the short analysis time (1.5 h). Consequently, the gating strategy for LSK cells in this group was appropriately adjusted for this group (Suppl. Fig. 7C, D). Overall, when comparing in vitro and in vivo studies, we replicated targeting improvements when using anti-cKit and anti-CD90, as well as identified in vivo targeting with anti-CD105, an effect that was not seen in vitro.

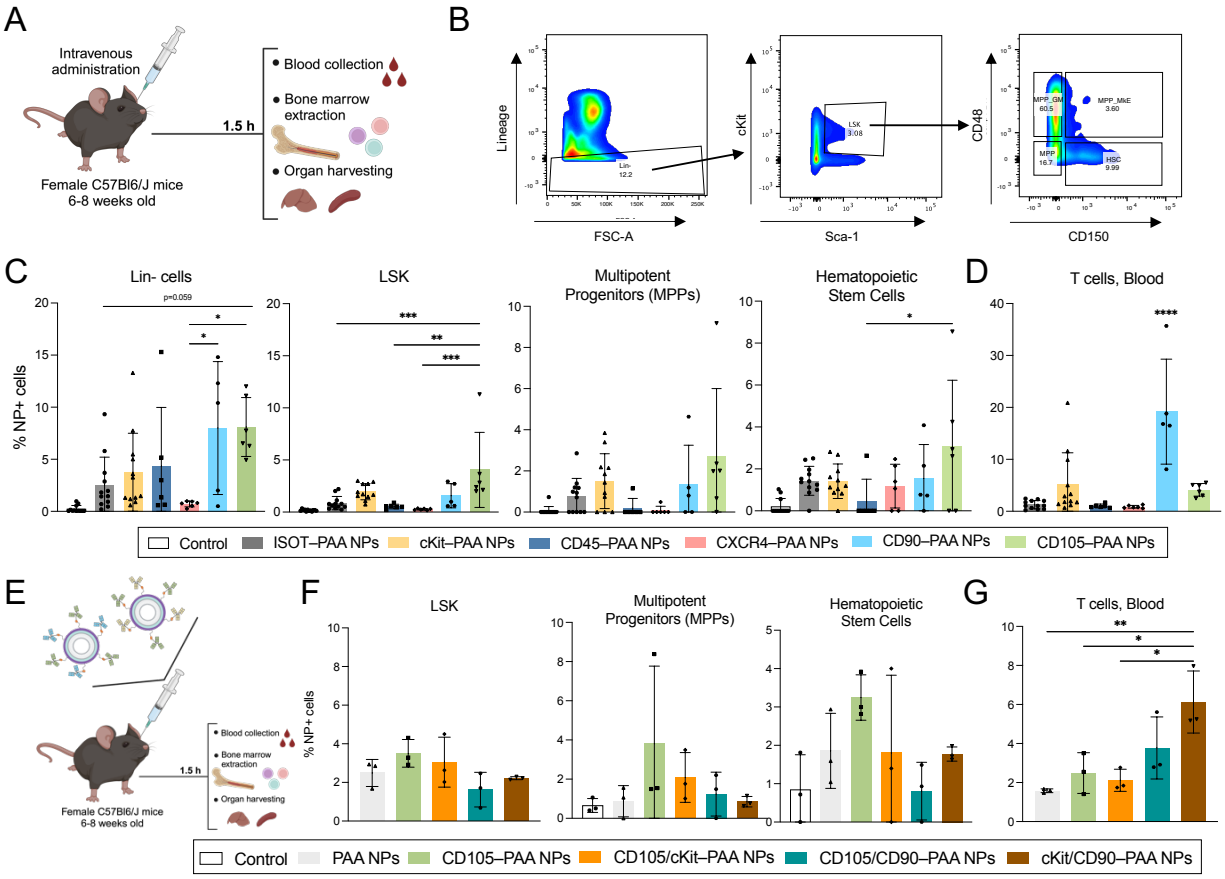

Fig. 4. Ab–PAA NPs improve NP targeting capacity of hematopoietic progenitors. (**A**) Timeline of in vivo study, in which Ab–PAA NPs are intravenously administered to mice blood, bone marrow, and organs are analyzed after 1.5 h. (**B**) Flow gating strategy for Lin- progenitors, Lin- cKit+ Sca-1+ cells (LSK), different multipotent progenitors (MPPs), and hematopoietic stem cells (HSCs). (**C**) Ab–PAA NP association to Lin-

cells, LSK cells, MPPs, and HSCs. (**D**) Ab–PAA NP association to blood-circulating T cells. (**E**) Timeline of in vivo study with dual-targeted Ab–PAA NPs. (**F**) NP association of the dual targeted Ab–PAA NPs to LSK, MPPs, and HSCs. (**G**) Dual targeted Ab–PAA NP association to blood-circulating T cells. Statistical analysis is a one-way ANOVA with Tukey correction among Ab–PAA NP groups (*$p<0.05$, **$p<0.01$, ***$p<0.005$, ****$p<0.001$). Bars represent mean, and each dot is one animal replicate ($n \geq 5$ per group in C and D; and $n = 3$ per group in F and G).

In parallel, we analyzed the interactions of the different Ab–PAA NPs with circulating blood cells. As a whole, cKit–, CD90–, and CD105–PAA NPs had higher interactions with leukocytes. More specifically, CD90– and CD105–PAA NPs were highly taken up by granulocytes and monocytes, and cKit–PAA NPs presented a higher interaction with circulating B cells (Suppl. Fig. 9). CD90–PAA NPs showed a significantly improved T cell association of 19.2%, opposite to the <5% association of any other Ab–PAA NP group (Fig. 4D). Among organs profiled, a higher NP signal was detected in both the liver and spleen for the cKit–, CD90– and CD105–PAA NP-treated groups (Suppl. Fig 10).

We explored to further improve the targeting capacity of CD105–PAA NPs with a dual targeting strategy combining the best performing candidates. For this, we prepared CD105/cKit–PAA NPs, CD105/CD90–PAA NPs, and cKit/CD90–PAA NPs, and compared NP uptake to the top-performing CD105-PAA NPs (Suppl. Fig. 11A–D). In vitro, the dual Ab combinations did not improve uptake over PAA NPs in WBM or Lin- cells (Suppl. Fig. 11E, F). Considering that in vitro evaluation overlooked the targeting effect of CD105–PAA NPs, we continued to evaluate the dual strategies in vivo. Mouse bone marrow cells, blood, and major organs were analyzed 1.5 h after intravenous administration. Flow cytometry revealed no significant differences among groups in WBM, Lin-, or LSK cells, with the single targeting strategy CD105–PAA NPs still outperforming (Fig. 4E and Suppl. Fig. 12A). Similar trends were captured for blood-circulating leukocytes, granulocytes, and monocytes (Suppl. Fig. 12B). The B-cell and T-cell tropism of anti-cKit- and anti-CD90-containing NPs, respectively, was retained within these combinations (Fig. 4F and Suppl. Fig. 12B). Notable differences in organ biodistributions were seen toward the spleen (Suppl. Fig. 13). Ultimately, we observe that single Ab targets, such as anti-CD105, improve HSPC targeting, similarly or even more strongly than combinations of Abs.

Targeting capacity is translated to human hematopoietic progenitors

To assess the translation of these Ab-conjugated NPs to a human context, we adapted our formulations to target human receptors. Abs against human cKit, CD45, CXCR4, CD90, and CD105 receptors were modified and conjugated to PAA NPs as previously described, with no notable changes to the physicochemical properties of the resulting Ab–PAA NPs (Suppl. Fig. 14). To evaluate human HSPC targeting, we treated human CD34+ cells with Ab–PAA NPs for 1.5 h, then analyzed NP uptake by flow cytometry. Overall, CD105–PAA NPs achieved the highest association to human CD34+ cells (Fig. 5A).

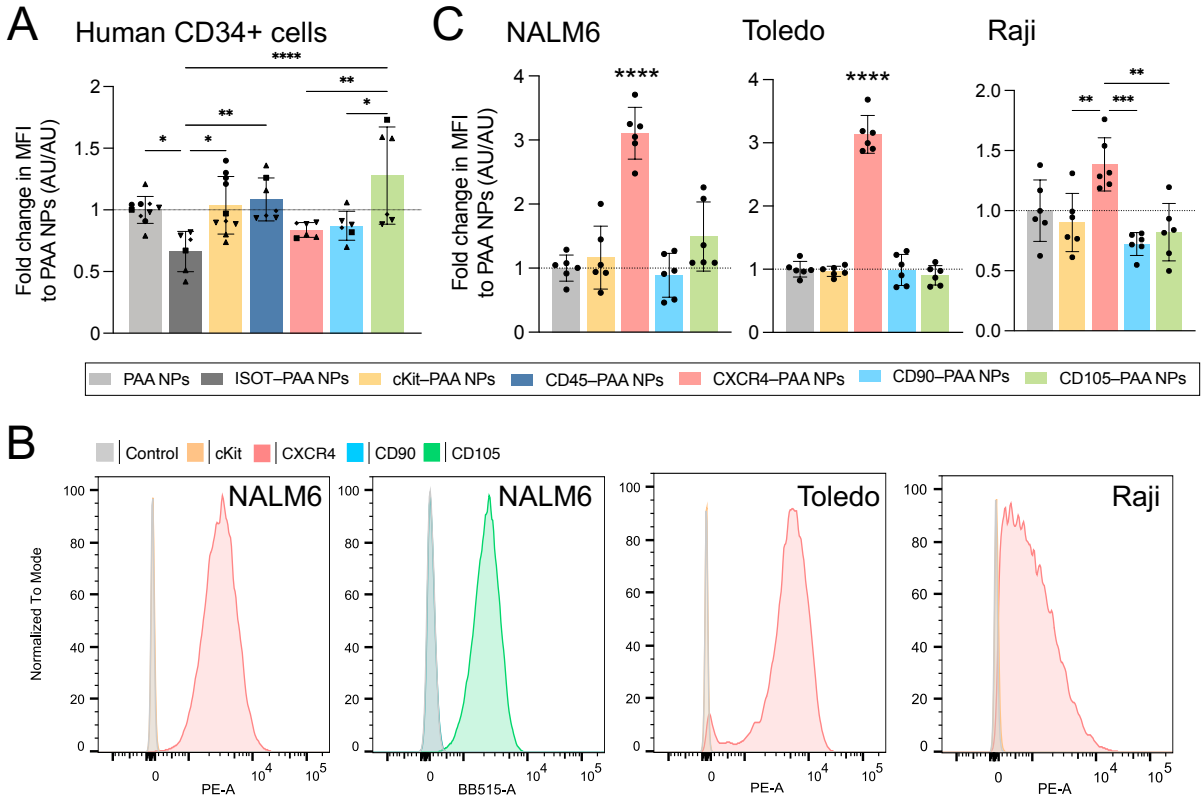

Fig. 5. Targeting of human hematopoietic progenitors. (**A**) Median fluorescence intensity (MFI) values for all Ab–LbL NP groups after 1.5 h of incubation in human CD34+ cells, normalized to PAA NPs. (**B**) Expression of surface receptors for cKit, CXCR4, CD90, CD105 on NALM6 cells, Toledo cells, and Raji cells. (**C**) Median fluorescence intensity (MFI) values after 1.5 h of incubation for anti-human Ab–PAA NPs, normalized to PAA NPs, in NALM6 cells, Raji cells, and Toledo cells. Statistical analysis is a one-way ANOVA with Tukey correction (**p<0.01, ***p<0.005, ****p<0.001). Bars represent mean with standard deviation. For (A) each shape represents a different donor (4 donors, 1-3 technical replicates). For (C) each dot is one technical replicate (2 biological replicates with 3 technical replicates each).

We then evaluated the capacity of the NP platform to target human leukemia progenitors. First, surface staining revealed that the CXCR4 receptor was most abundant in several leukemia cell lines (NALM6, Toledo, and Raji), while only the CD105 receptor was overexpressed in one of them (NALM6) (Fig. 5B and Suppl. Fig. 15A). In line with this, CXCR4–PAA NPs presented a 3.1- and 2.1-fold increase in association in NALM6 cells after 1.5 and 4 h of incubation, respectively, in comparison to PAA NPs. CD105–PAA NPs modestly improved this uptake (by 1.5- and 1.3-fold) (Fig. 5C and Suppl. Fig. 15B). Similarly, CXCR4-functionalization boosted NP uptake in Toledo cells by 3.1- and 2.5-fold, and in Raji cells by 1.4-fold (Fig. 5C and Suppl. Fig. 15B).

DISCUSSION

Effective drug delivery to HSPCs poses a great challenge for treating blood disorders, with major unmet needs for cost-effective accessible therapies and lowered off-target effects.[11,12] The first step in addressing these challenges is to mitigate the interaction with myeloid cells, such as

granulocytes and monocytes, to decrease the rapid clearance rates of NPs.[6] LbL NP formulations have previously demonstrated in vivo stability, long blood half-life, and lowered liver accumulation, highly desirable properties to be leveraged here.[17,46,47] Recently, a library of LbL NPs with varying carboxylic and sulfated polymer outer layers displayed varying degrees of association with primary non-cancerous cells.[48] In that work, PAA lowered in vitro NP interaction with macrophages and monocytes, while HA NPs and PLE-NPs showed intermediate values. In the current study, we found similar trends in vivo when evaluating these three polymer outer layers for association to blood-circulating immune cells. Indeed, PAA displayed minimal specificity toward these immune cells and major organs, as a result of its nature and lack of known binding partners. PLE showed an intermediate interaction with circulating granulocytes and monocytes, consistent with previous in vitro trends. In contrast, HA presented a significantly higher affinity for granulocytes and monocytes, which can be attributed to the high expression of its binding partner, the CD44 receptor, in immune cells.[49] Interestingly, HA NPs exhibited an increased association to T cells and to the spleen, suggesting its potential utility in other therapeutic avenues. Taken all together, PAA's lower interaction with granulocytes and monocytes and reduced organ accumulation led to its selection as the stealth outer layer of the Ab–LbL NPs used in this work.

With recent interest in leveraging HSPC-targeting strategies, we sought to better understand and compare which targeting moieties would be most advantageous to utilize across different hematological disorders. We rationally selected a library of HSPC-targeting Abs and optimized a method to facilitate highly efficient conjugation of these Abs to PAA NPs without major changes in the physicochemical properties of the resulting Ab–PAA NPs. In vitro, we saw strong correlations between Ab–PAA NP uptake trends in both WBM and Lin- cells. cKit–PAA NPs presented high association rates and were detected inside WBM cells at short time points, likely due to the rapid turnover of the receptor.[50] Functionalization of LNPs with cKit has shown great therapeutic promise, by inducing high transfection rates in HSPCs.[30,31] In the case of anti-CD45, some studies have shown an effective HSPC targeting capacity in vivo,[26,28] while others have not seen significant targeting or delivery improvements.[30] Here, our work suggests the low uptake of CD45–PAA NPs may be related to the receptor's low internalization. Other drug delivery strategies have exploited CD45 specifically to anchor nano- or microparticles on the surface of a variety of cells, and avoid their internalization.[51,52] Relative to anti-cKit and anti-CD45, less characterization of the HSPC-targeting properties of anti-CXCR4, anti-CD90, or anti-CD105 has been reported.[37,39,40] In our hands, only anti-CD90 demonstrated comparable or superior in vitro targeting properties to anti-cKit, although with significantly different percentage of receptors expressed by bone marrow cells and different internalization patterns. Similarly, although CXCR4–PAA NPs and CD90–PAA NPs appeared largely co-localized with WBM cell membranes, flow cytometry analysis demonstrated different uptake values among both systems. Previous studies with CD90-targeted systems had reported an increased internalization over time in leukocytes.[51] In vitro, CD105–PAA NPs did not show any improved association over PAA NPs. These studies highlight the importance of receptor internalization rate and pattern, beyond net receptor expression, in improving NP targeting an uptake by the cells of interest. Further characterization is needed to fully elucidate these factors.

Nevertheless, HSPC targeting in vivo is challenged by barriers not captured in vitro, from circulating immune cells to accessibility of the bone marrow niche. From our findings, anti-cKit and anti-CD90 showed some increased targeting both in vitro and in vivo, while anti-CD105 presents a unique in vivo targeting capacity not captured in vitro. The expression of the CD105 receptor on the surface of long-term repopulating HSCs, as well as on endothelial cells and in the bone marrow niche, might have facilitated CD105–PAA NP homing to bone marrow and targeting of HSPCs.[39,53,54] It is worth noting that other cKit–targeted systems in vivo have shown significant improvements in HSPC transfection in vivo, or a lung tropism not recapitulated here.[30,31] The differences in NP core, the Ab dose, or time of study, among others, could determine these differences. Based on this premise, we cannot rule out that anti-CD90 and anti-cKit are still strong candidates for HSPC targeting in vivo, but anti-CD105 is also a candidate to be considered when selecting an HSPC-targeting Ab. In parallel, we also observed enhanced targeting capacities with circulating blood cells for some Ab–PAA NPs, toward T cells with CD90–PAA NPs and to B cells using cKit–PAA NPs. The CD90 receptor is known to be highly expressed by peripheral T cells, while reports suggest the presence of the cKit receptor in certain B cell precursors.[57,58]

Aiming to further boost the targeting capacity of the platform, we prepared dual targeted Ab–PAA NPs by integrating the three most promising targeting moieties: cKit, CD90, and CD105. Previous reports have demonstrated that dual targeting strategies using ligands or bispecific Abs improve targeting capacities in preclinical and clinical contexts.[55,56] However, none of the Ab combinations we tested significantly improved the performance of the single targeting strategy of CD105–PAA NPs. The lack of a complementary effect observed with the dual-targeted Ab–PAA NPs could be attributed to differences in receptor expression and internalization patterns, as seen in vitro. Additionally, factors such as the distance between receptors, the ratios of antibodies used, and interactions with a greater number of off-target cells may explain these results.[55] Combining CD105–PAA NPs with HSPC mobilization strategies, administering multiple doses, or evaluating the system over longer time points are potential approaches to further increase the number of HSPCs targeted with this platform.

For a translational application, we then adapted the platform to target human receptors. Maintaining the physicochemical properties of PAA NPs, anti-human CD105–PAA NPs showed the highest association to healthy human CD34+ cells. This trend aligns with reports of anti-human CD105–NPs with good transfection rates, although the performance of this system was not directly compared to other targeting strategies.[31,40] In our experiments, there was some variability between cells from different donors, a potential consequence of changes in receptor expression between individuals that could be overcome with a personalized medicine approach to targeting therapies. Conversely, in many hematological malignancies, the CXCR4/CXCL12 axis has been reported to play an important role, presenting potential to be harnessed by the developed Ab–PAA platform.[59,60] Our studies confirmed the increased expression of CXCR4 receptor on the human pre-B cell lines NALM6 and Raji.[61,62] Although the CD105 receptor was also expressed by NALM6, only targeting the human CXCR4 receptor displayed a significant improvement in NP association to these lymphoblasts in vitro. Other studies have shown the potential of targeting CXCR4 for the treatment of both hematological cancers,[63–65] or solid tumors.[66] Given the diversity of cargo that the LbL NP platform can deliver,[18,19,21,67] this surface chemistry could direct chemotherapeutics of interest to these lymphoblasts, while maintaining

stealth properties that can decrease the off-target effects that usually limit the development of more effective anticancer therapies.

In sum, we have developed an Ab–LbL NP platform with stealth properties that is capable of targeting hematopoietic progenitors in healthy and diseased states by swapping a rationally selected targeting moiety. Our studies led us to identify the ideal HSPC targeting candidates with a context-dependent effectivity. These results unveil the importance of systematic studies to better understand how to leverage the biology of the tissues of interest into developing optimized drug delivery systems with potential therapeutic applications.

MATERIALS AND METHODS

Materials

Cholesterol, 1,2-distearoyl-sn-glycero-3-phospho-(1'-rac-glycerol) sodium salt (DSPG), 1,2-distearoyl-sn-glycero-3-phosphoethanolamine (DOPE), 1,2-distearoyl-sn-glycero-3-phosphocholine (DSPC), and 1,2-distearoyl-sn-glycero-3-phosphoethanolamine-N-(Cyanine 5) (DSPE-Cy5) were purchased from Avanti (Alabama, US).

Sulfo-cyanine dyes with NHS ester were purchased from Lumiprobe (Maryland, US). Tangential flow filtration filters were purchased from Repligen (Massachusetts, US).

Poly-L-arginine hydrochloride (19 kDa), poly-L-aspartic acid (14 kDa), and poly-L-glutamic acid (15 kDa) were purchased from Alamanda Polymers (Alabama, US). Hyaluronic acid (20 kDa) was purchased from LifeCore Biomedical (Minnesota, US). Polyacrylic acid (15 kDa) was purchased from Sigma-Aldrich (St. Louis, US).

Carboxylated polystyrene nanoparticles (FluoSpheres™, yellow-green) of 100 nm were purchased from Thermo Fisher Scientific (Massachusetts, US). Electron microscopy Carbon support film 200 mesh copper were obtained from Electron Microscopy Sciences (Pennsylvania, US). Goat-anti-Rat IgG (H+L0 6-nm gold nanoparticles were purchased from AURION Immuno Gold Reagents & Accessories (The Netherlands).

The antibodies rat-anti-mouse-cKit (CD117, clone 2B8), mouse-anti-mouse-CD45.2 (clone 104.2), rat-anti-mouse CD90.2 (Thy1.2, clone 30H12) and the corresponding isotypes (mouse IgG2a C1.19.4 and rat IgG2b LTF-2) were purchased from BioXCell (New Hampshire, USA). Antibody rat-anti-mouse-CXCR4 (CD184, clone 2B11), rat-anti-mouse CD105 (clone MJ7/18), mouse-anti-human CD45 (clone HI30), mouse-anti-human CXCR4 (CD184, clone 12G5), mouse-anti-human CD90 (Thy-1, clone 5E10), and mouse-anti-human CD105 (clone SN6) were purchased from Thermo Fisher Scientific (Massachusetts, US). Antibody mouse-anti-human-cKit (clone 104D2) was purchased from Peprotech (New Jersey, US).

Maleimide-PEG_3-tetraciclooctane, AZDye488–tetrazine, and MethylTetrazine-amine were purchased from Click Chemistry Tools (Arizona, US). N-hydroxysuccinimide (NHS) and N-(3-(dimethylamino)- propyl)-N-ethylcarbodiimide hydrochloride (EDC) were bought from Sigma-Aldrich (St. Louis, US),

Roswell Park Memorial Institute (RPMI 1640) cell culture media and penicillin/streptomycin were purchased from Corning (New York, US), and fetal bovine serum (FBS) was purchased from Gibco (Montana, US). StemSpan SFEM II serum-free, L-glutamine, recombinant human stem cell factor (SCF), recombinant mouse and human Fms-like tyrosine kinase 3/fetal liver kinase-2 (Flt3/Flk-2) ligands, recombinant mouse and human interleukin-3 (IL-3), recombinant mouse thrombopoietin (TPO) and human CD34+ cells were purchased from Stemcell Technologies (British Columbia, Canada). Recombinant mouse stem cell factor (mSCF) and recombinant human thrombopoietin (hTPO) were obtained from Peprotech (New Jersey, US).

The 8-Chamber Lab-Tek II Chambered #1.5 German Coverglass system, wheat germ agglutinin Alexa Fluor™ 555 and 647, and Hoescht 33342 trihydrochloride trihydrate were purchased from Invitrogen, (Massachusetts, US). A 0.01% poly-L-lysine solution was purchased from Sigma-Aldrich (St. Louis, US). Hank's balanced salt solution (HBSS) was obtained from Gibco (Montana, US), and 16% methanol-free formaldehyde from Thermo Fisher Scientific (Massachusetts, US).

Liposome synthesis

Liposomes were prepared as previously described.[68] Cholesterol and lipid stocks were made in only chloroform, or a chloroform : methanol : water [65 : 35 : 8 ratio] mixture, and combined in a flask at a mol ratio of 31 DSPC : 31 cholesterol : 31 DSPG : 7 DOPE or of 33 DSPC : 33 cholesterol

: 33 DSPG : 0.4 DSPE-Cy5. The lipids were dried into a thin film using a BUCHI RotoVap system under heat (55 °C, water bath) until completely dry (<30 mBarr). A Branson sonicator bath was heated to 65 °C, at which point the flask with the lipid film was partially submerged in the bath. A volume of ultrapure water was added to re-suspend the lipid film to a 2 mg lipid/mL solution. The liposome solution was sonicated on and off for 3 minutes, then transferred to an Avestin LiposoFast LF-50 liposome extruder. The extruder was connected to a Cole-Parmer Polystat Heated Recirculator Bath to maintain a temperature of 65 °C. The liposomes were extruded through nucleopore membranes by passing the solution through stacked 400 and 200 nm membranes, 100 nm, and 50 nm membranes. Fluorescently labeled liposomes were prepared either with a Cy5-dye, or via NHS-coupling of Sulfo-cyanine dyes with NHS ester handles to DOPE head group amines in sodium carbonate buffer (pH 8.5), stirred at room temperature overnight. Unconjugated dye was purified away from the labeled liposomes by tangential flow filtration (TFF).

Layer-by-Layer assembly

Nanoparticles were layered with polymers by adding an equal volume of NP core (at either 1 mg/mL or 0.5 mg/mL for HA) to the polymer solution under sonication for a few seconds.[68] The weight equivalents of polyelectrolyte used with respect to liposome core were of 0.25-0.33 for poly-L-arginine (PLR), 1-2 for hyaluronic acid (HA), 0.5-1 for poly-L-glutamic acid (PLE), and 0.125-0.33 for polyacrylic acid (PAA). For antibody-conjugated NPs, the final layer was a 1:1 mass ratio of unmodified PAA to methyltetrazine-modified PAA. Polyelectrolyte solutions were prepared in 50 mM HEPES (pH 7.4) and 40 mM NaCl, with the exception of HA, which was prepared in 2.5 mM HEPES.[68] The freshly layered particles were allowed to incubate at room temperature for 30 min, then purified using tangential flow filtration (TFF).

Polymer functionalization

Carboxylated polymer poly(acrylic acid) (PAA) wa modified with a methyltetrazine handle by NHS/EDC coupling chemistry. PAA was diluted in MES buffer (0.1 N, pH 6) to a concentration of 2 mg/mL. Then, solutions of methyltetrazine amine or 3-azidopropylamine, N-hydroxysuccinimide (NHS), and N-(3-(dimethylamino)- propyl)-N-ethylcarbodiimide hydrochloride (EDC) in the same buffer were added at a concentration 6.3-, 14.3-, and 143-fold times higher than the polymer, respectively. The solution was kept under magnetic stirring at 700 rpm for 4 h at room temperature and then dialyzed against NaCl 50 mM overnight, and up to 72 h against ultrapure water to remove free reactives (Spectrum Labs, regenerated cellulose membrane MW 3.5 kDa, California, US). The final polymer solution was frozen at −80 °C and lyophilized in a Labconco FreeZone Freeze Dryer System (Labconco, Missouri, USA).

Lyophilized polymers were resuspended in D_2O (Sigma-Aldrich, St. Louis, US), and analyzed by nuclear magnetic resonance (NMR). All NMR spectra were obtained using a three-channel Bruker Avance Neo spectrometer 500.34 MHz equipped with a 5 mm liquid-nitrogen cooled Prodigy broad band observe cryoprobe. Spectra were processed using MestReNova v14.2 (Mestrelab Research, Santiago de Compostela, Spain).

Purification by tangential flow filtration

Nanoparticles were purified using a Spectrum Labs KrosFlo II filtration system (Repligen, Massachusetts, USA). Hollow fiber filter membranes with 100 or 300 kDa molecular weight cutoffs made of modified polyethylene sulfone were used to remove free dyes or polymers from the nanoparticle solution. Samples were filtered at 13 mL/min or 80 mL/min (for 13 or 16 tubing, respectively), with an ultrapure water inlet line to replace the volume of waste permeate. Nanoparticles were considered purified after collecting at least 5 volume equivalents of waste (or 10 for the antibody-conjugated ones). Then, the sample was concentrated to the desired volume.

After each purification step, nanoparticle concentration was tracked based on a calibration curve of the initial liposome solution measuring the Cy5 fluorescent reading (excitation/emission 630/670 nm). For this purpose, nanoparticle samples were diluted in a 1 : 10 ratio in dimethyl sulfoxide, and read in a Tecan M1000 microplate reader (Tecan, Männedorf, Switzerland).

Nanoparticle characterization

The mean size and polydispersity index (PDI) of the nanoparticles were characterized by dynamic light scattering (DLS), and the zeta potential values by laser doppler anemometry, using a Malvern Zetasizer Pro (Malvern Panalytical, Malvern, UK). The measurements were done in triplicate, at 25 °C, with a red laser (landa=633nm) and a detection angle of 173°.

For cryo-electron microscopy (Cryo-EM), 3 µL of the NP sample and buffer containing solution were dropped on a lacey copper grid coated with a continuous carbon film and blotted to remove excess sample without damaging the carbon layer by Gatan Cryo Plunge III. Grid was mounted on a Gatan 626 single tilt cryo-holder equipped in the TEM column. The specimen and holder tip were cooled down by liquid-nitrogen. Imaging on a JEOL 2100 FEG microscope was done using minimum dose method that was essential to avoid sample damage under the electron beam. The microscope was operated at 200 kV and with a magnification in the ranges of 10,000–60,000 for assessing particle size and distribution. All images were recorded on a Gatan 2kx2k UltraScan CCD camera.

Antibody modification and conjugation to nanoparticles

Full antibodies were partially reduced by using 4-molar excess (to the antibody) of tris(2-carboxyethyl)-phosphine hydrochloride (TCEP) in a final buffer solution of 20 mM phosphate buffer, 150 mM NaCl, and 10 mM EDTA (pH 7.2). The mixture was incubated for 1 h at 37 °C, and then a 40-molar excess of the maleimide-PEG_3-TCO linker was added. The reaction was incubated for 1 h at room temperature, and then purified using a 7K Zeba™ Spin Column (Thermo Fisher Scientific, Massachusetts, US).

The number of linkers per antibody was approximated by conjugating an AZDye488™-tetrazine to the antibody and calculating the degree of labelling (DOL). For this, antibody-TCO was incubated with a 2-molar excess solution of the fluorophore for at least 1.5 h, and then purified with 7K Zeba™ Spin Column. Degree of labelling was quantified using a NanoDrop 1000 Spectrophotometer (Thermo Fisher Scientific, Massachusetts, US) reading the absorbance at 495 nm (AZDye488™-tetrazine ε = 83 000 M^{-1} cm^{-1}), and the protein absorbance at 280 nm for IgG.

For the conjugation of the antibody to nanoparticles, a 0.5 mg/mL solution of nanoparticles was mixed with 5% volume of the modified antibody at 1 mg/mL, and reacted for 1-2 h at room temperature or overnight at 4°C. After this time, unconjugated antibody was removed via TFF (10 volumes waste collected).

Protein concentrations were determined based on the protein absorbance at 280 nm for IgG using a NanoDrop 1000 Spectrophotometer. For concentrations of proteins conjugated to the nanoparticles, the colorimetric – bicinchoninic acid (BCA) assay (Thermo Fisher, Scientific, Massachusetts, US) was used. In this study, all samples were diluted to the same final nanoparticle concentration, to prevent interference of the dye with the assay.

Room temperature Transmission Electron Microscopy (TEM) and secondary staining of antibodies with gold nanoparticles

PS NPs were layered and conjugated to cKit antibody as described for liposomes. The purified cKit-PAA PS NPs and PAA PS NPs were analyzed by room temperature TEM. A 5 µL drop of NPs

(0.25 mg/mL, by fluorescence) was added to a 200 mesh copper grid coated with a continuous carbon film and let sit for 15 min. After this, the excess of NP was removed with a paper filter. Gold NPs were diluted 1/20 in 1x PBS with 0.1% BSA, pH 7.4 and the grid was incubated in a 100 µL droplet for 2 h at room temperature. After this time, the grid was washed six times in 1x PBS 0.1% BSA pH 7.4; six times in 1x PBS, and six times in deionized water. Then, grids were transferred to a droplet of uranyl acetate (3% in water) and washed in ten droplets of deionized water. Excess water was removed with a filter paper, and then stored at room temperature until imaged. A JEOL 2100 FEG microscope was used in the same conditions as previously described.

The number of gold NPs per NP core was counted using FIJI. The number of PS NPs and of gold NPs touching (on top or next to) them were counted, and an average of Ab (= 1 gold NP) per PS NP was estimated. The average of 13 images, containing a total of 334 PS NPs was used for these calculations. Counting was done manually. Given the conjugation yield of the cKit-PAA PS NPs was 3.3 times lower than for the cKit-PAA NPs with a liposomal core reported in the manuscript, the final number of Abs per NPs was corrected accordingly: multiplied by 3.3.

Bone marrow harvesting

Mice were euthanized following approved protocols. Mouse leg bones were isolated following stablished protocols [69,70]. Isolated bones were kept in cold RPMI, and then, epiphyses were cut, and bones were spun down on a 70-µm strainer for 20 min at 1,000 g. After this step, cells were incubated with Ammonium-Chloride-Potassium (ACK) lysing buffer (Thermo Fisher Scientific, Massachusetts, US) for 5 min at room temperature, and then white blood cells were collected by centrifugation at 300 g for 5 min. Media was aspirated, then cells were washed with cold PBS and isolated by centrifugation at 300 g for 5 min. For final experiments with bone marrow cells, the cell pellet was resuspended in mouse HSC media, containing StemSpan SFEM II serum-free medium supplemented with 1% L-glutamine, 1% penicillin/streptomycin, 100 ng/mL mouse SCF, 100 ng/mL mouse Flt3/Flk-2 ligand, 20 ng/mL of mouse IL-3, and 50 ng/mL mouse TPO. Cells were seeded at a density of 50,000 cells per 200 µL per well of a 96 well plate.

Human CD34+ cell experiments

Human CD34+ cells were thawed and cultured overnight in at a concentration of 10^6 cells/mL in human HSC media: StemSpan SFEM II serum-free medium supplemented with 1% L-glutamine, 1% penicillin/streptomycin, 100 ng/mL human SCF, 100 ng/mL human Flt3/Flk-2 ligand, 20 ng/mL of human IL-3, and 50 ng/mL human TPO. The next day, cells were harvested, counted, and resuspended in human HSC media without cytokines at a density of 50,000 cells per 200 µL per well of a 96 well plate.

Human leukemia cells

Human NALM6, clone G5, Toledo, and Raji cells were cultured according to manufacturer specifications in RPMI-1640 media supplemented with 10% FBS, 1% penicillin/streptomycin. Cells were incubated at 37 °C with an atmosphere with 100% humidity and 5% CO_2. Cells were authenticated using STR profiling and tested for mycoplasma. For in vitro uptake studies, 40,000 NALM6 cells were seeded in 200 µL per well, and 40,000 Toledo or Raji cells were seeded in 100 µL per well.

In vitro uptake studies

For flow cytometry experiments, cells were plated as previously described in a 96-well plate and let to grow overnight. Next day, a solution of the nanoparticles in ultrapure water were added, as a 10% of the well volume. Nanoparticles and cells were incubated for 0.5, 1.5, or 4 h. After this, cells were transferred to a non-treated 96-well plate, washed with PBS, stained for live/dead with

Zombie Violet™ Fixable Viability Kit (BioLegend, California, US). For bone marrow cells, cells were then blocked for 10 min at room temperature (TruStain FcX™ (anti-mouse CD16/32) Antibody) and stained with an FITC anti-mouse Lineage Cocktail (BioLegend, California, US) for 20 min at 4 °C. Cells were then washed and resuspended in FACS buffer to be read in a flow cytometer BD LSR II or BD Fortessa (BD Biosciences, New Jersey, US). FlowJo™ v10 (BD Biosciences, New Jersey, US) was used to analyze the resulting data. Median fluorescence intensity (MFI) values are represented as the fold increase to the untargeted PAA NPs [$MFI_{Ab\text{-}NPs}$ / $MFI_{PAA\ NPs}$].

Confocal imaging

The chambered slides were coated with a solution of 0.01% poly-L-lysine solution for 15 min, and then aspirated. Chambers were allowed to fully dry overnight at 37 ºC. In parallel, mouse bone marrow cells were cultured on 96-well plates at 50,000 cells per 200 µL per well. The next day, cells were incubated with Cy5-labelled NPs for 1.5 h at 37 ºC, 5% CO_2. After this, cells were spun down, and washed with PBS twice. Then, cells were transferred to the poly-L-lysine coated chambered slides and let incubate for 15 min at room temperature. Cells were then fixed with 4% formaldehyde in PBS for 15 min at room temperature, and washed three times with HBSS over 15 min. Samples were stained with 10 µg/mL wheat germ agglutinin labelled with Alexa Fluor™ 555 for 10 min. Then, they were washed again with PBS three times over 15 min, stained with 1.5 µg/mL Hoechst 33342 for 2 min. Finally, samples were washed with PBS and stored at 4 ºC and protected from light until imaging. Imaging was conducted in an Olympus FV1200 Laser Scanning Confocal Microscope with an inverted IX83 microscope equipped with 405, 440, 473, 559, and 635 nm lasers. Images were acquired with 100x objective. Final image analysis was done with FIJI.

Animal husbandry

All animal experiments were approved by the MIT Committee for Animal Care (protocol 221000434). Healthy female C57BL/6J mice 6−8 weeks old were obtained from The Jackson Laboratory and housed at the Koch Institute animal facility at MIT, in groups of up to 5 mice per cage. Animals were allowed to acclimate for at least 72 h before any manipulation. Routine husbandry was provided with the assistance of the MIT Division of Comparative Medicine (DCM) staff. Animals were given ad libitum access to IsoPro RMH 3000 chow (LabDiet) and water and were maintained in 12 h light-dark cycles.

In vivo nanoparticle dosing

Female C57BL/6J mice 6−8 weeks old were injected retro-orbitally with Cy5-labeled LbL NPs at a lipid concentration of 0.75 mg/mL; and an Ab concentration of up to 30 mg/kg (<0.2 mg/mL) in 200 µL. All NPs were dosed in sterile-filtered isotonic 5% dextrose. At the corresponding time points, blood was collected via retro-orbital bleeding (not in the eye of injection), and mice were euthanized.

Organ harvesting and fluorescence analysis

Organs were harvested, immersed in RPMI, dried and weighed, then transferred to cold PBS. Organs were kept on ice for all intermediate periods. To determine fluorescent signal, excised organs were dried and imaged on a Xenogen IVIS Imaging System (PerkinElmer, Massachusetts). Fluorescence is reported as the total radiant efficiency (in [p/s] / [$\mu W/cm^2$]), normalized by the values of the control organs.

Blood analysis by flow cytometry

Blood was collected in a BD Microtainer® tube with K2 EDTA (BD Biosciences, New Jersey, US). Within 1h of the collection, tubes were centrifuged for 20 min at 1,000 g. Supernatant was

removed, and remaining cells were incubated in ACK lysing buffer for 5 min, then centrifuged for 5 min at 300 g. This process was repeated until a white cell pellet withwas obtained. Cells were then resuspended in 1 mL of RPMI and left in ice until flow preparation. Within 3 h, blood cells were counted, and 10^6 cells per mouse were plated in a 96-well plate. Cells were washed with PBS, stained for live/dead with Zombie Aqua™ Fixable Viability Kit, then blocked for 10 min at room temperature (TruStain FcX™) and stained with a cocktail containing FITC-CD45 (clone 30-F11, 103107), Pacific Blue™-B220 (clone RA3-6B2, 103230), PE-CD3 (clone 17A2, 100205), and PE/Cyanine7-CD11b (clone M1/70, 101215) in Cell Staining Buffer (BioLegend, California, US) for 25 min at 4 ºC. All staining ratios used followed manufacturer recommendations. Cells were then washed twice and resuspended in Cell Staining Buffer to be analyzed in a flow cytometer BD Fortessa (BD Biosciences, New Jersey, US). Compensation was calculated with compensation beads (Thermo Fisher Scientific, Massachusetts, US). FlowJo™ v10 (BD Biosciences, New Jersey, US) was used to analyze the resulting data. Gating strategy is shown in Suppl. Fig. 1.

Flow cytometry analysis of bone marrow cells from nanoparticle-dosed mice

Bone marrow was extracted as previously described in the “Bone marrow harvesting” section. Cells were resuspended in 4 mL of cold PBS and left in ice until flow preparation. Within 3 h, bone marrow cells were counted, and $3x10^6$ cells per mouse were plated in a 96-well plate. Cells were washed with PBS, stained for live/dead with Zombie Aqua™ Fixable Viability Kit, then blocked for 10 min at room temperature (TruStain FcX™) and stained with a cocktail containing Alexa Fluor ® 700 Lineage cocktail (clones 17A2; RB6-8C5; RA3-6B2; Ter-119; M1/70; 133313), FITC-cKit (clone ACK2, 135115), Pacific Blue™-Sca-1 (clone E13-161.7, 122519), PE-CD48 (clone HM48-1, 103405), PE/Cyanine7-CD150 (clone TC15-12F12.2, 115914) in Cell Stanining Buffer (BioLegend, California, US) for 25 min at 4 ºC. All staining ratios used followed manufacturer recommendations. Cells were then washed twice and resuspended in Cell Staining Buffer to be analyzed in a flow cytometer BD Fortessa (BD Biosciences, New Jersey, US). Compensation was calculated with compensation beads (Thermo Fisher Scientific, Massachusetts, US). FlowJo™ v10 (BD Biosciences, New Jersey, US) was used to analyze the resulting data. Gating strategy is shown in Suppl. Fig. 7.

Statistical analysis

Data analysis was performed using GraphPad Prism version 9.1 (GraphPad Inc.). Statistical analysis is described in each figure caption. Data were expressed as the mean ± standard deviation (SD). p values of 0.05 or less were considered statistically significant.

References

[1] E. Laurenti, B. Göttgens, *Nature* **2018**, *553*, 418.
[2] M. Cavazzana, F. D. Bushman, A. Miccio, I. André-Schmutz, E. Six, *Nat. Rev. Drug Discov.* **2019**, *18*, 447.
[3] G. Ferrari, A. J. Thrasher, A. Aiuti, *Nat. Rev. Genet.* **2021**, *22*, 216.
[4] B. A. Anthony, D. C. Link, *Trends Immunol.* **2014**, *35*, 32.
[5] R. R. Jenq, M. R. M. Van Den Brink, *Nat. Rev. Cancer* **2010**, *10*, 213.
[6] C. M. Drysdale, T. Nassehi, J. Gamer, M. Yapundich, J. F. Tisdale, N. Uchida, *Cell Stem Cell* **2021**, *28*, 191.
[7] R. A. Morgan, D. Gray, A. Lomova, D. B. Kohn, *Cell Stem Cell* **2017**, *21*, 574.
[8] High-dose AAV gene therapy deaths, *Nat. Biotechnol.* **2020**, *38*, 910.
[9] J. Guo, X. Luan, Z. Cong, Y. Sun, L. Wang, S. L. McKenna, M. R. Cahill, C. M. O'Driscoll, *J. Controlled Release* **2018**, *286*, 154.
[10] J. Li, Q. Wang, Y. Han, L. Jiang, S. Lu, B. Wang, W. Qian, M. Zhu, H. Huang, P. Qian, *J. Hematol. Oncol.J Hematol Oncol* **2023**, *16*, 65.
[11] A. Lieber, H.-P. Kiem, *Mol. Ther.* **2023**, *31*, 2823.
[12] R. Murugesan, K. V. Karuppusamy, S. Marepally, S. Thangavel, *Front. Genome Ed.* **2023**, *5*, 1148693.
[13] T. G. Dacoba, S. Anthiya, G. Berrecoso, I. Fernández-Mariño, C. Fernández-Varela, J. Crecente-Campo, D. Teijeiro-Osorio, F. Torres Andón, M. J. Alonso, *Adv. Funct. Mater.* **2021**, *31*, 2009860.
[14] E. Samaridou, J. Heyes, P. Lutwyche, *Adv. Drug Deliv. Rev.* **2020**, *154–155*, 37.
[15] X. Zhang, T. Liang, Q. Ma, *Drug Deliv.* **2021**, *28*, 655.
[16] N. Boehnke, P. T. Hammond, *JACS Au* **2022**, *2*, 12.
[17] Z. J. Deng, S. W. Morton, E. Ben-Akiva, E. C. Dreaden, K. E. Shopsowitz, P. T. Hammond, *ACS Nano* **2013**, *7*, 9571.
[18] L. Gu, Z. J. Deng, S. Roy, P. T. Hammond, *Clin. Cancer Res.* **2017**, *23*, 7312.
[19] A. E. Barberio, S. G. Smith, S. Correa, C. Nguyen, B. Nhan, M. Melo, T. Tokatlian, H. Suh, D. J. Irvine, P. T. Hammond, *ACS Nano* **2020**, *14*, 11238.
[20] S. W. Morton, Z. Poon, P. T. Hammond, *Biomaterials* **2013**, *34*, 5328.
[21] N. Nabar, T. G. Dacoba, G. Covarrubias, D. Romero-Cruz, P. T. Hammond, *Proc. Natl. Acad. Sci.* **2024**.
[22] N. Boehnke, K. J. Dolph, V. M. Juarez, J. M. Lanoha, P. T. Hammond, *Bioconjug. Chem.* **2020**, *31*, 2211.
[23] N. Boehnke, S. Correa, L. Hao, W. Wang, J. P. Straehla, S. N. Bhatia, P. T. Hammond, *Angew. Chem. Int. Ed.* **2020**, *59*, 2776.
[24] J. P. Straehla, C. Hajal, H. C. Safford, G. S. Offeddu, N. Boehnke, T. G. Dacoba, J. Wyckoff, R. D. Kamm, P. T. Hammond, *Proc. Natl. Acad. Sci.* **2022**, *119*, e2118697119.
[25] K. Y. Choi, S. Correa, J. Min, J. Li, S. Roy, K. H. Laccetti, E. Dreaden, S. Kong, R. Heo, Y. H. Roh, E. C. Lawson, P. A. Palmer, P. T. Hammond, *Adv. Funct. Mater.* **2019**, *29*, 1900018.
[26] R. Palchaudhuri, B. Saez, J. Hoggatt, A. Schajnovitz, D. B. Sykes, T. A. Tate, A. Czechowicz, Y. Kfoury, F. Ruchika, D. J. Rossi, G. L. Verdine, M. K. Mansour, D. T. Scadden, *Nat. Biotechnol.* **2016**, *34*, 738.
[27] M. L. Hermiston, Z. Xu, A. Weiss, *Annu. Rev. Immunol.* **2003**, *21*, 107.
[28] R. Palanki, J. S. Riley, S. K. Bose, V. Luks, A. Dave, N. Kus, B. M. White, A. S. Ricciardi, K. L. Swingle, L. Xue, D. Sung, A. S. Thatte, H. C. Safford, V. S. Chaluvadi, M. Carpenter, E. L. Han, R. Maganti, A. G. Hamilton, K. Mrksich, M. B. Billingsley, P. W. Zoltick, M.-G. Alameh, D. Weissman, M. J. Mitchell, W. H. Peranteau, *Proc. Natl. Acad. Sci.* **2024**, *121*, e2400783121.
[29] J. Lennartsson, L. Rönnstrand, *Physiol. Rev.* **2012**, *92*, 1619.
[30] D. Shi, S. Toyonaga, D. G. Anderson, *Nano Lett.* **2023**, *23*, 2938.
[31] L. Breda, T. E. Papp, M. P. Triebwasser, A. Yadegari, M. T. Fedorky, N. Tanaka, O. Abdulmalik, G. Pavani, Y. Wang, S. A. Grupp, S. T. Chou, H. Ni, B. L. Mui, Y. K. Tam, D. Weissman, S. Rivella, H. Parhiz, *Science* **2023**, *381*, 436.
[32] C. E. Edling, B. Hallberg, *Int. J. Biochem. Cell Biol.* **2007**, *39*, 1995.
[33] A. Philippidis, *Hum. Gene Ther.* **2023**, *34*, 177.
[34] R. Möhle, F. Bautz, S. Rafii, M. A. Moore, W. Brugger, L. Kanz, *Blood* **1998**, *91*, 4523.
[35] P. Singh, K. S. Mohammad, L. M. Pelus, *Stem Cells* **2020**, *38*, 849.

[36] A. S. Jørgensen, V. Daugvilaite, K. De Filippo, C. Berg, M. Mavri, T. Benned-Jensen, G. Juzenaite, G. Hjortø, S. Rankin, J. Våbenø, M. M. Rosenkilde, *Commun. Biol.* **2021**, *4*, 569.
[37] K. Berckmueller, J. Thomas, E. A. Taha, S. Choo, R. Madhu, G. Kanestrom, P. B. Rupert, R. Strong, H.-P. Kiem, S. Radtke, *Mol. Ther.* **2023**, *31*, 2901.
[38] H. Parhiz, D. Weissman, H.-P. Kiem, S. Radtke, C. Peterson, *CD-90 targeted lipid nanoparticles*, **2024**.
[39] S.-K. Kays, K. B. Kaufmann, T. Abel, C. Brendel, H. Bonig, M. Grez, C. J. Buchholz, S. Kneissl, *Stem Cells Dev.* **2015**, *24*, 714.
[40] H. F. Moffett, M. E. Coon, S. Radtke, S. B. Stephan, L. McKnight, A. Lambert, B. L. Stoddard, H. P. Kiem, M. T. Stephan, *Nat. Commun.* **2017**, *8*, 389.
[41] W. Craig, R. Kay, R. L. Cutler, P. M. Lansdorp, *J. Exp. Med.* **1993**, *177*, 1331.
[42] O. W. Rokhlin, M. B. Cohen, H. Kubagawa, M. Letarte, M. D. Cooper, *J. Immunol.* **1995**, *154*, 4456.
[43] P. M. Kelly, C. Åberg, E. Polo, A. O'Connell, J. Cookman, J. Fallon, Ž. Krpetić, K. A. Dawson, *Nat. Nanotechnol.* **2015**, *10*, 472.
[44] L. M. Herda, D. R. Hristov, M. C. Lo Giudice, E. Polo, K. A. Dawson, *J. Am. Chem. Soc.* **2017**, *139*, 111.
[45] N. Boehnke, J. P. Straehla, H. C. Safford, M. Kocak, M. G. Rees, M. Ronan, D. Rosenberg, C. H. Adelmann, R. R. Chivukula, N. Nabar, A. G. Berger, N. G. Lamson, J. H. Cheah, H. Li, J. A. Roth, A. N. Koehler, P. T. Hammond, *Science* **2022**, *377*, eabm5551.
[46] Z. Poon, J. B. Lee, S. W. Morton, P. T. Hammond, *Nano Lett.* **2011**, *11*, 2096.
[47] S. Correa, E. C. Dreaden, L. Gu, P. T. Hammond, *J. Controlled Release* **2016**, *240*, 364.
[48] S. Correa, N. Boehnke, A. E. Barberio, E. Deiss-Yehiely, A. Shi, B. Oberlton, S. G. Smith, I. Zervantonakis, E. C. Dreaden, P. T. Hammond, *ACS Nano* **2020**, *14*, 2224.
[49] S. S. M. Lee-Sayer, Y. Dong, A. A. Arif, M. Olsson, K. L. Brown, P. Johnson, *Front. Immunol.* **2015**, *6*.
[50] A. Nagamachi, J. Kikuchi, A. Kanai, Y. Furukawa, T. Inaba, *Haematologica* **2020**, *105*, e325.
[51] L. Tang, Y. Zheng, M. B. Melo, L. Mabardi, A. P. Castaño, Y.-Q. Xie, N. Li, S. B. Kudchodkar, H. C. Wong, E. K. Jeng, M. V. Maus, D. J. Irvine, *Nat. Biotechnol.* **2018**, *36*, 707.
[52] N. Kapate, M. Dunne, N. Kumbhojkar, S. Prakash, L. L.-W. Wang, A. Graveline, K. S. Park, V. Chandran Suja, J. Goyal, J. R. Clegg, S. Mitragotri, *Proc. Natl. Acad. Sci.* **2023**, *120*, e2221535120.
[53] C.-Z. Chen, M. Li, D. De Graaf, S. Monti, B. Göttgens, M.-J. Sanchez, E. S. Lander, T. R. Golub, A. R. Green, H. F. Lodish, *Proc. Natl. Acad. Sci.* **2002**, *99*, 15468.
[54] K. J. G. Kenswil, P. Pisterzi, G. Sánchez-Duffhues, C. Van Dijk, A. Lolli, C. Knuth, B. Vanchin, A. C. Jaramillo, R. M. Hoogenboezem, M. A. Sanders, J. Feyen, T. Cupedo, I. G. Costa, R. Li, E. M. J. Bindels, K. Lodder, B. Blom, P. K. Bos, M.-J. Goumans, P. Ten Dijke, E. Farrell, G. Krenning, M. H. G. P. Raaijmakers, *Cell Stem Cell* **2021**, *28*, 653.
[55] P. Guo, J. Yang, D. Liu, L. Huang, G. Fell, J. Huang, M. A. Moses, D. T. Auguste, *Sci. Adv.* **2019**, *5*, eaav5010.
[56] U. Brinkmann, R. E. Kontermann, *Science* **2021**, *372*, 916.
[57] S. M. M. Haeryfar, D. W. Hoskin, *J. Immunol.* **2004**, *173*, 3581.
[58] G. Balciunaite, R. Ceredig, S. Massa, A. G. Rolink, *Eur. J. Immunol.* **2005**, *35*, 2019.
[59] L. Su, Z. Hu, Y. Yang, *Cell Prolif.* **2021**, *54*, e13076.
[60] L. M. Jonart, J. Ostergaard, A. Brooks, G. Fitzpatrick, L. Chen, P. M. Gordon, *Br. J. Haematol.* **2023**, *201*, 459.
[61] H. J. Wester, U. Keller, M. Schottelius, A. Beer, K. Philipp-Abbrederis, F. Hoffmann, J. Šimeček, C. Gerngross, M. Lassmann, K. Herrmann, N. Pellegata, M. Rudelius, H. Kessler, M. Schwaiger, *Theranostics* **2015**, *5*, 618.
[62] X. Dong, L. Mu, X. Liu, H. Zhu, S. Yang, X. Lai, H. Liu, H. Feng, Q. Lu, B. S. Zhou, H. Chen, G. Chen, J. F. Lovell, D. Hong, C. Fang, *Adv. Funct. Mater.* **2020**, *30*, 2000309.
[63] V. Pallarès, U. Unzueta, A. Falgàs, L. Sánchez-García, N. Serna, A. Gallardo, G. A. Morris, L. Alba-Castellón, P. Álamo, J. Sierra, A. Villaverde, E. Vázquez, I. Casanova, R. Mangues, *J. Hematol. Oncol.J Hematol Oncol* **2020**, *13*, 36.
[64] C. Chittasupho, C. Aonsri, W. Imaram, *Bioorganic Chem.* **2021**, *107*, 104601.
[65] X.-H. Ren, C. Xu, L.-L. Li, Y. Zuo, D. Han, X.-Y. He, S.-X. Cheng, *J. Controlled Release* **2022**, *343*, 645.
[66] P. Guo, J.-O. You, J. Yang, M. A. Moses, D. T. Auguste, *Biomaterials* **2012**, *33*, 8104.

[67] N. Nabar, T. G. Dacoba, G. Covarrubias, D. Romero-Cruz, P. T. Hammond, *Proc. Natl. Acad. Sci.* **2024**, *121*, e2307809121.
[68] S. Correa, N. Boehnke, E. Deiss-Yehiely, P. T. Hammond, *ACS Nano* **2019**, *13*, 5623.
[69] X. Liu, N. Quan, *BIO-Protoc.* **2015**, *5*.
[70] S. R. Amend, K. C. Valkenburg, K. J. Pienta, *J. Vis. Exp.* **2016**, 53936.

Acknowledgments: This work was supported, in part, by the Bill and Melinda Gates Foundation (grant ID INV-021791 and INV-050202). Under the grant conditions of the Foundation, a Creative Commons Attribution 4.0 Generic License has already been assigned to the Author Accepted Manuscript version that might arise from this submission. All data underlying the results are available as part of the article and no additional source data are required. Research was also funded by the Koch Institute's Marble Center for Cancer Nanomedicine. N.N is supported by the NSF Graduate Research Fellowship Program under Grant No. 2141064. Any opinions, findings, and conclusions or recommendations expressed in this material are those of the authors and do not necessarily reflect the views of the NSF. We would like to thank the Koch Institute's Robert A. Swanson (1969) Biotechnology Center for technical support, specifically the Flow Cytometry Core, Microscopy Core, Nanotechnology and Nanomaterials core, High Throughput Sciences core, and the ES Cell and Transgenics Facility. Figures in this manuscript were partially created using https://www.Biorender.com. We would additionally like to thank Dr. Margaret Billingsley and Dr. Nicholas Lamson for their help in reviewing this manuscript.

Competing interests: PTH is a co-founder and member of the board of LayerBio, a member of the Scientific Advisory Board of Moderna, and a member of the Board of Alector, Advanced Chemotherapy Technologies, and Burroughs-Welcome Fund. All other authors report no competing interests.